Modulational instability in vector exciton-polariton condensates with photonic spin-orbit coupling

Edmond B. Madimabe, Conrad B. Tabi, Camus G. Latchio Tiofack, and Timoléon C. Kofané

Modulational Instability in Vector Exciton-Polariton Condensates with Photonic Spin-Orbit Coupling

Edmond B. Madimabe,[1, *] Conrad B. Tabi,[1, †] Camus G. Latchio Tiofack,[2, ‡] and Timoléon C. Kofané[1, 3, 4, §]

[1]*Department of Physics and Astronomy, Botswana International University*
of Science and Technology, Private Mail Bag 16 Palapye, Botswana
[2]*Faculty of Sciences, University of Maroua, P.O. Box 814, Maroua, Cameroon*
[3]*Laboratory of Mechanics, Department of Physics, Faculty of Science,*
University of Yaoundé I, P.O. Box 812, Yaoundé, Cameroon
[4]*Centre d'Excellence Africain en Technologies de l'Information et de la Communication, University of Yaoundé I, Cameroon*
(Dated: April 13, 2023)

The paper demonstrates the existence of modulational instability (MI) in nonlinear exciton-polariton condensates (EPCs). A set of coupled two-dimensional (2D) driven-dissipative Gross-Pitaevskii (GP) equations describing the spin-up and spin-down polaritons, containing the photonic spin-orbit (SO) coupling and the rate equations describing the density of incoherent excitonic reservoir density is reduced to a system of two coupled 2D complex Ginzburg-Landau (2DCGL) equations, with saturable nonlinearities for complex polariton order parameters, thanks to the adiabatic approximation and small density fluctuations approximation. The analytical approach relies on the linear stability analysis of continuous waves (CWs) to derive an expression for the growth rate and conduct a parametric study of MI. The effect of different parameters on the growth rate spectrum is discussed with an emphasis on the photonic SO coupling and the pumping power. The predictions are verified against a direct simulation of the 2DCGL equations, and excellent agreement is found. The emergence of solitonic clusters manifests the evolution of MI. Phase diagrams on a MI spectrum for the CWs are presented against the magnetic field (B) and SO coupling strength (σ), based on which the dynamical behaviors of the emerging structures are debated, along with their response to changing σ and B. The results suggest that the photonic SO coupling and the magnetic field constitute efficient tools for nonlinear mode selection and characterization via the MI process and are equally important in any eventual experimental realization of such a process in the studied EPC system.

I. INTRODUCTION

Theoretical and experimental descriptions of the nonlinear effects in EPCs in microcavities [1] have been the subject of recent studies, opening many promising directions for the future, such as the possibility of novel functionalities for information processing devices [2]. EPCs or cavity polaritons appear as elementary excitations formed by the strong coupling of a photonic mode of a planar semiconductor and an excitonic resonance in a quantum well embedded in the antinode of a cavity mode [3]. In this respect, the polaritons are a mixture of material excitations (excitons) with light (photons). However, unlike the atomic Bose-Einstein condensates (BECs), the dynamics of the EPCs are nonconservative due to the presence of strong losses of excitons and photons due to material and cavity imperfections.

To treat such EPCs skillfully, fundamental studies have been carried out on the specificities of polariton condensates and model equations governing the dynamical properties. From these perspectives, using the open-dissipative GP as a model equation, which describes an incoherently pumped BEC coupled to the exciton reservoir, it has been predicted that spatial localization of the steady-state of the polariton BEC is a dissipative soliton [4]. Strongly localized quasicompactons in dissipative EPCs have been obtained analytically and numerically [5]. Interestingly, considering the densities of active and inactive reservoirs, the tight-binding approximation has been used to explain the increasing density modulation in 1D valley with disorder [6]. Ring-shaped condensates of the polaritons with nonzero angular momenta have been reported [7]. It has been shown that vortices possess two winding numbers being either integer or half-integer simultaneously, and that four half vortices have the smallest energy [8]. Remarkably, a stochastic classical field equation coupled to a rate equation for the exciton reservoir has been used to describe the dynamics of the long-range spatial coherence [9]. On the other hand, the possibility of creating oblique dark half-solitons in EPCs has been discussed [10]. Moreover, the photoluminescence spectrum of the excitations of EPCs, taking into account reservoir effects, has been calculated [11].

In the meantime, stable solutions have been observed numerically in semimagnetic EPCs [12]. Also, different regimes of EPCs have been found using a fixed points analysis [13]. Furthermore, dark spatial solitons have been predicted inside the band gap of an EPC in a 1D periodic potential [14]. In a perturbative regime of sufficiently small reservoir excitations, it has been shown that

* me21100032@studentmail.biust.ac.bw
† Corresponding author: tabic@biust.ac.bw
‡ glatchio@yahoo.fr
§ tckofane@yahoo.com

the dynamics of the macroscopic wavefunction, coupled to a rate equation for the exciton reservoir density, can be described by the Korteweg-de Vries equation with linear loss [15]. Indeed, under the combined effect of pumping and losses, the stationary state of polariton BECs is characterized by a steady flow in the outward radial direction [16]. It has been reported that the interplay between the repulsive exciton-exciton interaction and cavity dispersion can generate Gap solitons [17, 18]. Let us mention that the mechanisms of polarization dephasing and relaxation have been examined on a stochastic polarization in EP BECs under pulsed excitations [19]. The intrinsic lifetime of half-vortices in a spinor cavity EPCs and the texture of the vortices have been analyzed [20]. In addition, it has been revealed that the quenching of the Zeeman splitting is due to a phase synchronization of spin-up and spin-down polarized EPCs [21]. Indeed, an analogy between magnetic monopoles and half-integer topological defects in spinor polariton condensates has been established [22]. Next, the power-dependent transition of EPs to a dynamical condensate has been characterized [23]. A device for deterministically producing bright coherent non-Gaussian light from EPCs has been proposed taking advantage of the polariton-polariton interactions [24].

In this paper, we start with coupled generalized GP equations and rate equations for the incoherent excitonic reservoir density describing the dynamics of spinor polariton condensates trapped in ring-shaped confining potentials created by excitonic reservoirs [25]. The generalized GP equations take into account the photonic effective spin-orbit interaction, which is due to the transverse electric and transverse magnetic photonic modes splitting (TE-TM splitting) and the exciton Zeeman splitting, which is produced by an external magnetic field. Next, a system of two coupled 2D cubic CGL equations with saturable nonlinearities for both complex polariton order parameters are derived through an adiabatic elimination of the reservoir density, where the reservoir relaxation rate is fast compared to other time scales of condensate evolution [26]. Indeed, conditions under which the adiabatic reduction of the open-dissipative GP equation to the cubic CGL equation is justified have been derived [27]. Here, we explore the MI of spinor polariton condensates trapped in ring-shaped confining potentials, both analytically by the linear stability analysis of the MI of CW solutions and numerically by the split-step Fourier method and direct integrations of the corresponding 2D cubic CGL equations with saturable nonlinearities. In addition, particular attention will be devoted to various physical effects on MI, such as photonic spin-orbit interactions, optical pumping powers, effects of polariton condensate interaction with incoherent exciton of the same and the orthogonal polarizations, and the effect of nonlinear polariton-polariton interactions are comprehensively discussed. We also want to note that using Bogoliubov-de Gennes theory, the boundary of a modulationaly unstable region in the parameter space was determined within

the open-dissipative GP model [28]. Effects of polariton energy relaxation and the inhomogeneous pumping profile have been taken into account in the study of the MI process [29]. It has been shown that the mechanism of optical bistability in microcavities is associated with the MI process between odd and even states of the trapping potential [30]. Strong peaks of MI in semiconducting excitonic media have been found to possess gain orders of magnitude larger than that in the case of optical fibers [31]. In addition, when the pump width of the Gaussian laser beam is comparable to the unstable wavelength in which MI arises, the self-rotation of the condensate has been observed [32]. MI analysis has been used to describe a diffusive behavior of the Goldstone mode in BEC of exciton-polaritons [33]. MI of uniform states has been analyzed in the dual-core optical waveguide as an emulator for the EP system in the lossless limit [34]. MI was also predicted in two-component helicoidal spin-orbit-coupled dissipative BECs whose dynamics are described by coupled cubic CGL equations [35]. The impact of the left- and right-handed helicoidal spin-orbit couplings on MI of Bose-Bose mixtures has been discussed [36].

The paper is organized as follows. In Sec. II, we present 2D coupled generalized GP equations and rate equations for the incoherent excitonic reservoir density describing the dynamics of confined nonequilibrium polariton condensates, from which a system of two coupled 2D cubic CGL equations with saturable nonlinearities for both complex polariton order parameter functions is derived using the adiabatic approximation. In Sec. III, the linear stability analysis of the MI of CW solutions of the coupled cubic 2DCGL equations with saturable nonlinearities is formulated. An expression for the MI growth rate is proposed, from which the parametric occurrence of MI is discussed. Then, in Sec. IV, the stability analysis predictions are fully confronted with numerical results obtained via direct numerical integrations of the cubic 2DCGL partial differential equations with saturable nonlinearities. Finally, in Sec. V, we conclude with a summary of the main results of this contribution.

II. MODEL AND LINEAR STABILITY ANALYSIS

A. Model

Evolution of the polariton condensate and the exciton reservoir is described by the coupled driven-dissipative equation of the Gross Pitaevskii type and the rate equations with dimensionless form [25]

$$
i\frac{\partial \psi_l}{\partial t} = -\frac{1}{2}\Delta\psi_l + (-1)^{3-l}B\psi_l + (gn_l + \tilde{g}n_{3-l})\psi_l
$$
$$
+ (|\psi_l|^2 + h|\psi_{3-l}|^2)\psi_l + i\left(n_l - \frac{1}{2}\right)\psi_l \quad \text{(1a)}
$$
$$
+ \sigma\left(\frac{\partial}{\partial x} + i(-1)^l\frac{\partial}{\partial y}\right)^2 \psi_{3-l},
$$

$$\frac{\partial n_l}{\partial t} = I_l - \left(\Gamma + G|\psi_l|^2\right)n_l, \quad l=1,2. \quad (1b)$$

$\Delta = \partial^2/\partial x^2 + \partial^2/\partial y^2$ is the Laplacian operator in 2D. The quantities ψ_l $(l=1,2)$ are dimensionless order parameter functions describing the spin-up $(l=1)$ and spin-down $(l=2)$ polaritons, respectively. $n_l = R\rho_l/2\gamma_c$ $(l=1,2)$ are dimensionless exciton densities describing the density of incoherent excitons that create both effective gain and repelling potential for coherent polaritons, where R is the coupling parameter between reservoirs and condensates. γ_c is the condensate dumping rate and ρ_l describes the densities of incoherent excitons. $B = g\mu_B/2\hbar\gamma_c$ is the dimensionless magnetic field. In fact, the magnetic field B shifts the eigenfrequencies of the spin-up and spin-down polaritons in the opposite directions, leading to the eigenfrequencies difference $g_e\mu_B B$, where μ_B is the Bohr magneton, and g_e is the effective excitonic g factor. The dimensionless coefficients $g = 2g_R/\hbar R$ and $\tilde{g} = 2\tilde{g}_R/\hbar R$ are the parameters accounting for the polariton condensate interactions with incoherent excitons of the same and the orthogonal polarization, respectively, where g_R and $\tilde{g}_R$ are the coefficients of nonlinear interaction between polaritons and incoherent reservoir excitons. $\hbar$ is the usual Planck's constant. $h_{cp} = g_x/g_c$ is the dimensionless coefficient accounting for nonlinear cross-polarization interactions, where g_c and g_x are the nonlinear coefficients of interaction between polaritons belonging to the same and to the orthogonal polarizations. $\sigma = (m_t - m_l)/(m_t + m_l)$ is the strength of the TE-TM splitting that is also known as the photonic effective spin interaction, with m_t and m_l being the transverse and longitudinal masses of the polaritons. $\Gamma = \gamma_R/\gamma_c$ is the dimensionless decay rate of incoherent excitons, where γ_R denotes the reservoir dumping rate. $G = \hbar R/g_c$ accounts for the depletion of the exciton reservoir due to condensation into the coherent part, and, finally, $I_l = RP_l/2\gamma_c$ are the dimensionless pumping powers in the right $(l=1)$ and left $(l=2)$ circular polarization, with P_l representing the pumping powers.

In the typical case where the characteristic relaxation rate Γ of the reservoir is much faster than all scales, one can adiabatically eliminate n_1 and n_2, respectively. The adiabatic elimination procedure consists of finding the following stationary solutions

$$n_l = \frac{I_l}{\Gamma + G|\psi_l|^2}, \quad l=1,2. \quad (2)$$

Substituting Eqs.(2) into the set (1a), we derive a system of two coupled 2D cubic dissipative Gross-Pitaevskii

equations with saturable nonlinearities which reads as

$$\begin{aligned} i\frac{\partial \psi_l}{\partial t} = &-\frac{1}{2}\left(\frac{\partial^2}{\partial x^2} + \frac{\partial^2}{\partial y^2}\right)\psi_l + \left(B - \frac{i}{2}\right)\psi_l \\ &+ \left(\frac{(g+i)I_l}{\Gamma + G|\psi_l|^2} + \frac{\tilde{g}I_{3-l}}{\Gamma + G|\psi_{3-l}|^2}\right)\psi_l \\ &+ (|\psi_l|^2 + h|\psi_{3-l}|^2)\psi_l \\ &+ \sigma\left(\frac{\partial}{\partial x} + i(-1)^l\frac{\partial}{\partial y}\right)^2\psi_{3-l}, \quad l=1,2. \end{aligned} \quad (3)$$

Based on the set of Eqs. (3), we will now investigate the MI phenomenon. Before we proceed, precision should be made that the adiabatic approximation is a widely used technique that assumes that the reservoir follows the condensate dynamics instantaneously and is expected to be accurate if the reservoir decay time $1/\gamma_R$ is the fastest time scale [27]. In other terms, the reservoir density $n_l(x,t)$ $(l=1)$ is stationary and adiabatically follows the change of $|\psi_l(x,t)|^2$ as given by Eq. (2) of the manuscript. This indubitably leads to the manuscript's Eq.(2) and to the coupled CGL Eqs. (3) used in the rest of the work. We then understand that even though the reservoir density is stationary in this case, the changes made to the system due to the adiabatic approximation make the coefficients of the coupled CGL equations dependent on the now constant pumping rates I_1 and I_2, along with other parameters like G and Γ that are also related to the stationary reservoir. This explains why their impact on the growth rate spectrum will be studied in the next section.

B. Linear stability analysis of CWs

Next, we use the standard linear stability analysis to study the MI phenomenon in a driven-dissipative multistable system. The steady-state solutions of Eqs. (3), corresponding to the CW signal, can be written as $\psi_l = \sqrt{n_{l0}}e^{-i\mu t}$ $(l=1,2)$, where n_{l0} are uniform densities, respectively and μ is the common chemical potential of both polariton components. They are related by the following relation,

$$\begin{aligned} \mu = &B(-1)^{3-l} + \frac{gI_l}{\Gamma + Gn_l} + \frac{\tilde{g}I_{3-l}}{\Gamma + Gn_{3-l}} + n_{l0} \\ &+ hn_{3-l0} + i\frac{I_l}{\Gamma + Gn_{3-l}} - \frac{i}{2}, \quad l=1,2. \end{aligned} \quad (4)$$

The linear stability of the steady state can be examined by introducing the perturbed fields of the following form

$$\psi_l = \left(\sqrt{n_{l0}} + \delta\psi_l\right)e^{-i\mu t}, \quad l=1,2 \quad (5)$$

where $\delta\psi_l$ are small perturbations, with $|\delta\psi_l| \ll \sqrt{n_{l0}}$ being complex fields. Substituting Eqs. (5) into Eqs. (3) and linearizing around the unperturbed solutions leads

to the following equations for the perturbed fields

$$i\frac{\partial(\delta\psi_l)}{\partial t} = -\frac{1}{2}\left(\frac{\partial^2}{\partial x^2} + \frac{\partial^2}{\partial y^2}\right)\delta\psi_l + \sigma\left(\frac{\partial^2}{\partial x^2} - \frac{\partial^2}{\partial y^2}\right)\delta\psi_{3-l}$$

$$+ 2i(-)^l\sigma\frac{\partial^2(\delta\psi_{3-l})}{\partial x\partial y} + n_{l0}\left(\delta\psi_l^* + \delta\psi_l\right)$$

$$+ h\sqrt{n_{l0}n_{3-l0}}\left(\delta\psi_{3-l}^* + \delta\psi_{3-l}\right)$$

$$- \frac{gI_l n_{l0}G\left(\delta\psi_l^* + \delta\psi_l\right)}{(\Gamma + Gn_{l0})^2} - \frac{\tilde{g}I_{3-l}\sqrt{n_{l0}n_{3-l0}}G\left(\delta\psi_{3-l}^* + \delta\psi_{3-l}\right)}{(\Gamma + Gn_{3-l0})^2}$$

$$- i\frac{I_l n_{l0}G\left(\delta\psi_l^* + \delta\psi_l\right)}{(\Gamma + Gn_{l0})^2}, \quad l = 1,2, \tag{6}$$

where $\delta\psi_l^*$ are the complex conjugates of the perturbed fields $\delta\psi_l$. Now, we assume the following solutions for

the perturbed fields

$$\delta\psi_l = a_{l1}e^{i(K_1 x + K_2 y - \Omega t)}$$
$$+ a_{l2}^* e^{-i(K_1 x + K_2 y - \Omega^* t)}, \quad l = 1,2 \tag{7}$$

where K_1 and K_2 are the wave numbers, Ω is a complex modulation frequency of perturbations modulating the carrier signal, and a_{l1} and a_{l2} are constant complex amplitudes, respectively. The substitution of solutions (7) into Eqs. (6) gives a linear homogeneous system of equations in terms of a_{l1} and a_{l2}, i.e.,

$$M \times [a_{11}, a_{12}, a_{21}, a_{22}]^T = 0, \tag{8}$$

where M is a 4×4 matrix given by

$$M = \begin{bmatrix} S_1 + e + f + \Omega & S_1 + e & S_2 + g - d & S_2 \\ S_1 - e & S_1 - e + f - \Omega & S_2 & S_2 + g + d \\ S_4 + g + d & S_4 & h + S_3 + f + \Omega & S_3 + h \\ S_4 & S_4 + g - d & S_3 - h & S_3 - h + f - \Omega \end{bmatrix} \tag{9}$$

whose elements are given in the **Appendix A**. Since we seek a nontrivial solution of the system in Eq. (8), we require that $\text{Det}(M) = 0$. After some straightforward calculations, we obtain the following nonlinear dispersion relation

$$\Omega^4 + P_3\Omega^3 + P_2\Omega^2 + P_1\Omega + P_0 = 0 \tag{10}$$

with $P_\nu(\nu = 0,1,2,3)$ being given in the **Appendix B**.

The procedure adopted in this paper to study the MI growth rate comprises two steps: the analytical procedure and the full numerical one. **(i)** For the analytical procedure, the following four solutions are obtained for Eq.(10):

$$\Omega_{1,2} = -\frac{P_3}{4} - \frac{1}{2}\sqrt{\frac{1}{4}P_3^2 - \frac{2}{3}P_2 + \Lambda}$$

$$\pm \frac{1}{2}\sqrt{-\frac{4}{3}P_2 + \frac{1}{2}P_3^2 - \Lambda + \frac{P_3^3 - 4P_3P_2 + 8P_0}{4\sqrt{\frac{1}{4}P_3^2 - \frac{2}{3}P_2 + \Lambda}}},$$

$$\Omega_{3,4} = -\frac{P_3}{4} + \frac{1}{2}\sqrt{\frac{1}{4}P_3^2 - \frac{2}{3}P_2 + \Lambda}$$

$$\pm \frac{1}{2}\sqrt{-\frac{4}{3}P_2 + \frac{1}{2}P_3^2 - \Lambda - \frac{P_3^3 - 4P_3P_2 + 8P_0}{4\sqrt{\frac{1}{4}P_3^2 - \frac{2}{3}P_2 + \Lambda}}}, \tag{11}$$

where

$$\Lambda = \frac{1}{3}\left(\sqrt[3]{\frac{\Delta_2 + \sqrt{\Delta_2^2 - 4\Delta_1^3}}{2}} + \frac{\Delta_1}{\sqrt[3]{\frac{\Delta_2 + \sqrt{\Delta_2^2 - 4\Delta_1^3}}{2}}}\right),$$

with $\Delta_1 = P_2^2 - 3P_3P_1 + 12P_0$, and $\Delta_2 = 2P_2^3 - 9P_3P_2P_1 + 27P_3^2P_0 + 27P_1^2 - 72P_2P_0$. The set of solutions (11) are such that the frequencies $\Omega_l(l = 1,2,3,4)$ are dependent on the values of the parameters that constitute the coefficients of the dispersion relation. This implies that Ω_l may be positive, negative, or even complex, depending on values of such parameters. Additionally, the growth rate spectrum $\zeta(K_1, K_2)$ can be positive or negative, and its sign can be specified for a particular set of values of the wavenumbers K_1 and K_2. Negative growth rate values refer to stability, a case where the system experiences vanishing of $\text{Im}(\Omega_l)$ as $t \to \infty$. Oppositely, positive values are related to the instability of the CWs, since the perturbation diverges without limit as time increases. Therefore, the sign of $\text{Im}(\Omega_l)$ informs about the stability of the CWs, and the regions of instability are commonly known as the growth rate spectrum, where the growth rate is given by $\zeta_1 = \text{Im}(\Omega_1) > 0$, or $\zeta_2 = \text{Im}(\Omega_2) > 0$, or $\zeta_3 = \text{Im}(\Omega_3) > 0$, or $\zeta_4 = \text{Im}(\Omega_4) > 0$. **(ii)** For the full numerical procedure, instead of repeating four times the calculation of finding the imaginary part of each of the solutions, one extracts numerically the largest value among such imaginary parts and compute the maximum growth rate such that

$$\zeta(\Omega) = \max\{\zeta_1, \zeta_2, \zeta_3, \zeta_4\}. \tag{12}$$

More explicitly, the latter expression indicates that the calculations for the MI growth rate, performed in the next section, are based on the highest positive imaginary part of the four solutions given in Eq.(11).
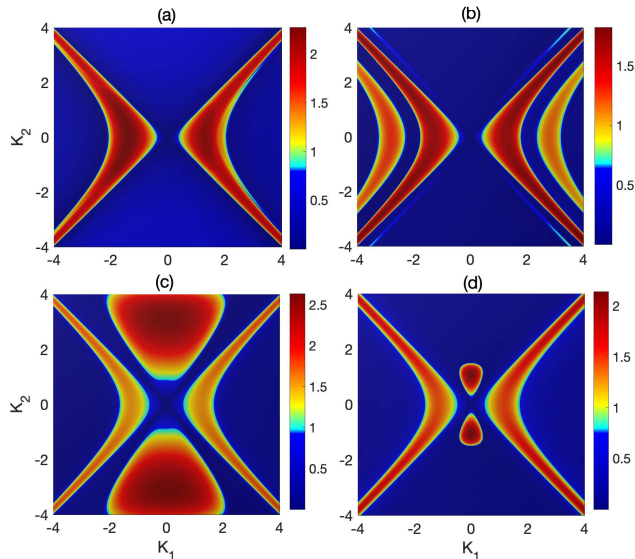
Figure 1. The panels show the variation of the MI gain $\zeta(\Omega)$ in the $(K_1, K_2)-$plane for (a): $\sigma = 0.03$, (b): $\sigma = 0.5$, (c): $\sigma = 0.7$, and (d): $\sigma = 0.9$, with the other parameters being $I = 3.0$ $G = 1.1$, $g = 3.64$, $\tilde{g} = -0.364$, $h = -0.1$, and $n_{10} = n_{20} = n_0 = 1$.
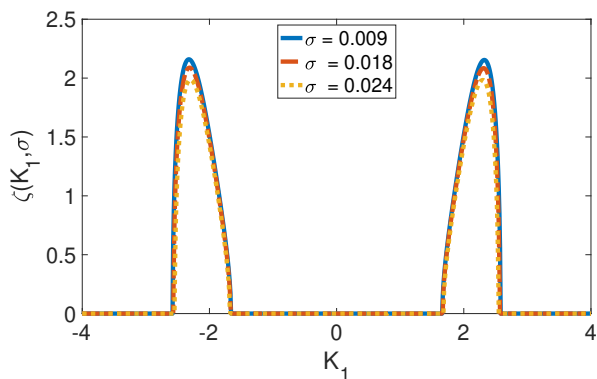

Figure 2. The panels show the variation of the MI gain $\zeta(\Omega)$ versus the wavenumber K_1 under the effect of weak values of the photonic SO coupling for $K_2 = 2$ and the parameter values $I = 3.0$ $G = 1.1$, $g = 3.64$, $\tilde{g} = -0.364$, $h = -0.1$, and $n_{10} = n_{20} = n_0 = 1$.

III. PARAMETRIC ANALYSIS OF THE GROWTH RATE OF INSTABILITY

We know that the MI is extremely sensitive to the system parameters. In the current context, it is evident from the dispersion relation (10) that the growth rate is highly influenced by the photonic SO interaction strength (σ) and the pumping power ($I_1 = I_2 = I$). The absence of the magnetic field parameter B in the dispersion relation for instability means that it cannot contribute to the properties of the MI spectrum. In this paper, we would like to discuss the interplay between differ-
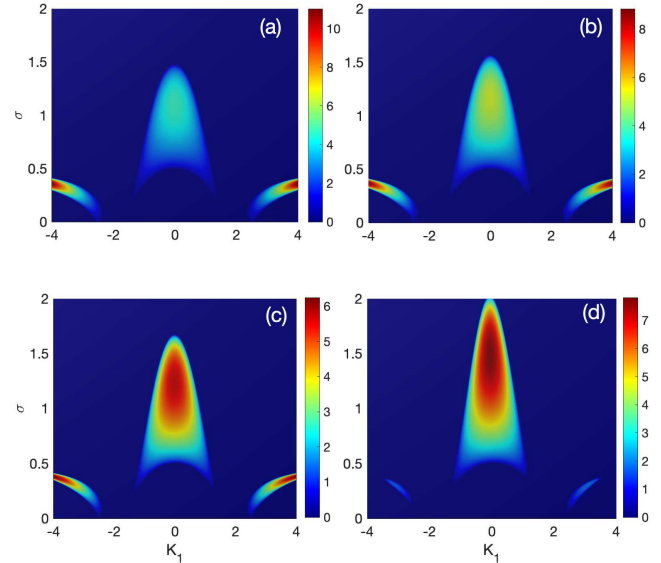

Figure 3. The panels show the variation of the MI gain $\zeta(\Omega)$ versus the perturbation wavenumber K_1 and the photonic SO coupling strength σ for (a): $I_1 = I_2 = 1$, (b): $I = 3$, (c): $I_1 = I_2 = 5$, and (d): $I_1 = I_2 = 6$, with $K_2 = 1.5$, $G = 1.1$, $g = 3.64$, $\tilde{g} = -0.364$, $h = -0.1$, and $n_{10} = n_{20} = n_0 = 1$.

ent system parameters in the instability spectrum. For a comprehensive study, we consider different combinations of the physical parameters in question and present the other cases. For the calculations, we consider two polariton condensate components with equal densities $n_{10} = n_{20} = n_0$. For convenience, we assume these densities to equal one, that is, $n_0 = 1$. Also, we only consider the case of equal pumping power in both polarizations $I = I_1 = I_2$. Thus, following the mathematical calculation pertaining to the nonlinear dispersion relation corresponding to the system's instability, we dedicate the subsequent sections to the study of various effects in the instability spectra of our system.

A. Effect of the photonic SO interactions (σ) on MI

In order to highlight the effect of the photonic SO coupling, we have first represented, in Fig. 1, the MI growth rate in the $(K_1, K_2)-$plane for different values of σ. From the initial spectrum obtained in Fig. 1(a), with $\sigma = 0.03$, one notices the appearance of additional instability regions with σ increasing. Particularly, the asymmetric lobes along K_2, when $\sigma = 0.7$ get shrunk for $\sigma = 0.9$ as shown in Fig. 1(d). Interestingly, one obtains from Fig. 3 that the pumping power affects the MI growth rate, enhancing the instability. It is, in fact, shown in the $(K_1, \sigma)-$plane that, with increasing I, the minor tongue of instability appearing in Fig. 3(a) tends
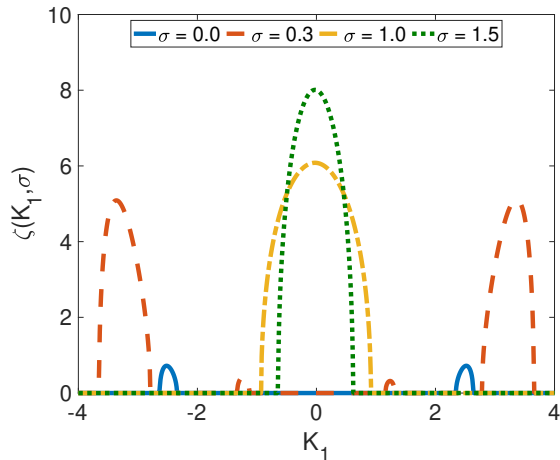
Figure 4. The panel shows the cross-section of the MI growth rate $\zeta(\Omega)$ versus the perturbation wavenumber K_1 for $K_2 = 1.5$. This corresponds to the results of Fig. 3(c), with the lines corresponding to increasing values of the photonic SO coupling strength σ. The rest of the parameter values are: $I_1 = I_2 = 5$, $G = 1.1$, $g = 3.64$, $\tilde{g} = -0.364$, $h = -0.1$, and $n_{10} = n_{20} = n_0 = 1$.

to become the major instability zone, therefore, eliminating the initial lateral zones of high growth rate. The cross-section of Fig. 3 is depicted in Fig. 4, where it is revealed that instability takes place even in the absence of the photonic SO coupling. Increasing σ, as already seen in Fig. 3, enhances the growth of instability via a single instability hump, with maximum situated at $K_1 = 0$. More interestingly, cross-sections of the MI growth rate of Fig. 1 are represented in Fig. 2 for weak values of the photonic SO coupling and $K_2 = 2$, which shows that the point $(K_1, K_2) = (2, 2)$ is a suitable point capable of giving rise to the disintegration of the plane wave solutions. This particular example is treated in the numerical simulations.

B. Effect of input powers ($I = I_1 = I_2$) on MI

Since it is contained in the coefficients of the nonlinear dispersion relation (8), the constant input power is expected to contribute to the MI growth rate. This is effective from Fig. 5, where the growth rate spectrum is addressed in the (K_1, I)−plane. Following the same procedure as in the previous cases, the different panels correspond to increasing values of the photonic SO coupling σ. Initially, for $\sigma = 0.03$, the instability is two major symmetric lobes between which one perceives two minor lobes of instability that disappear when I gets stronger, leaving only the major zones [see Fig. 5(a)]. Interestingly, all input power values make the instability growth rate available. While the two major lobes of Fig. 5(a) persist, there appears between them a large zone of instability with the maximum at $K_1 = 0$, which originates
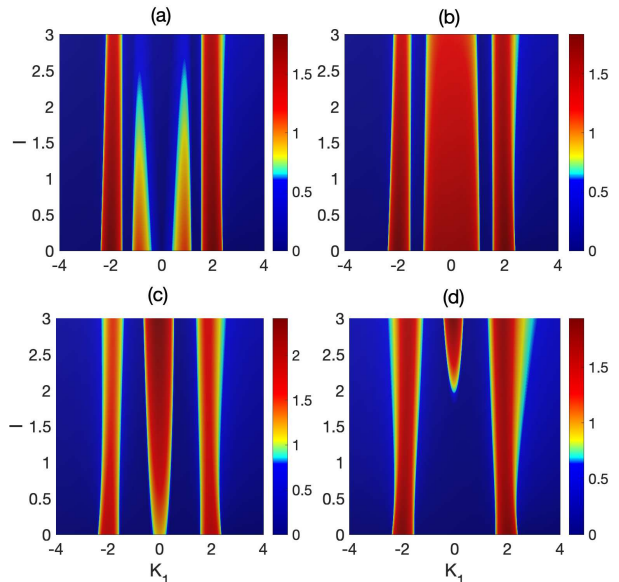

Figure 5. The panels show the distribution of the MI gain $\zeta(\Omega)$ versus the perturbation wavenumber K_1 and the input power $I = I_1 = I_2$ for (a): $\sigma = 0.03$, (b): $\sigma = 0.5$, (c): $\sigma = 0.7$, and (d): $\sigma = 0.9$, with the other parameters being $K_2 = 1.5$, $G = 1.1$, $g = 3.64$, $\tilde{g} = -0.364$, $\Gamma = 3$, $h = -0.1$, and $n_{10} = n_{20} = n_0 = 1$.

from the combination of the previous two minor lobes [see Fig. 5(b)]. The central major instability zone shrinks for $\sigma = 0.7$ and expands with I increasing, while its maximum takes place for $I > 1.5$. In the process, its satellite sidebands lose intensity but get enhanced for $\sigma = 0.9$. The central lobe is restricted to high values of I, i.e., $I > 2$, which implies that high pumping powers promote MI in polariton systems. However, the magnitude of the growth rate is highly affected by the changes in the photonic SO coupling, and the lobes, with I increasing, become asymmetric. This can be explained by the fact that in the optical fiber relying on the NLS equation, the MI gain is usually a quadratic function of the perturbation frequency, corresponding to a symmetric MI gain with respect to the origin. This has been reported even in the presence of other additional physical effects such as higher-order dispersion, higher-order nonlinearities, walk-off effects, and cross-phase modulation, to cite a few [37–39]. Nevertheless, recent studies on materials with spin-orbit coupling have shown that new effects can affect the symmetric properties of the MI gain spectrum. For example, asymmetric lobes of instability have been recently obtained by including the helicoidal spin-orbit coupling in BECs, where the strong effect of the gauge amplitude causes the MI gain spectrum to be asymmetric, while weak values of the same effect support symmetric lobes of the MI gain spectrum [40]. Very recently, the same behaviors of the MI gain were reported in Bose-Bose mixtures in the presence of the Rashba and Dresselhaus
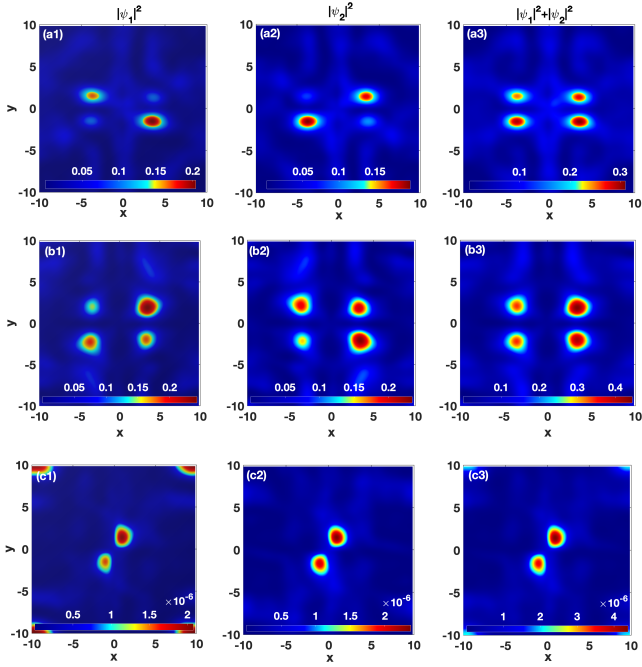
Figure 6. Development of MI, with the panels $(aj)_{j=1,2,3}$, $(bj)_{j=1,2,3}$ and $(cj)_{j=1,2,3}$ corresponding respectively to $\sigma = 0.009$, $\sigma = 0.018$, $\sigma = 0.024$ and the other parameters being: $I_1 = I_2 = 2$, $G = 1.1$, $g = 3.64$, $\tilde{g} = -0.364$, $K_1 = K_2 = 2$, $\Gamma = 3$, $h = -0.1$, $n_{10} = n_{20} = n_0 = 1$, and $B = 0.02$. From left to right, the columns correspond to $|\psi_1|^2$, $|\psi_2|^2$, and $(|\psi_1|^2 + |\psi_2|^2)$.

Figure 7. The panels show the numerically generated phase diagrams in the $(B, \sigma)-$plane for: (a) $I_1 = I_2 = 0.4$, (b) $I_1 = I_2 = 0.6$, (c) $I_1 = I_2 = 1.2$ and (d) $I_1 = I_2 = 2$. The wavenumber K_1, K_2, and the initial densities n_0 keep their values used to generate Fig. 6, while the other parameter values are: $G = 1.1$, $g = 3.64$, $\tilde{g} = -0.364$, $\Gamma = 3$, and $h = -0.1$. The points A_0, A_1, and A_2 corresponds to values of B and σ was used to generate Fig. 6, while the points A_3, A_4 and A_5 were used to corroborate the results of Figs. 8 and 9. The point C_0 was used to test the stability of the CW solutions, which gives the results of Fig. 10. MI indicates the region of instability, and MS (modulational stability) indicates the region of stability.

spin-orbit couplings [41], and also under the helicoidal SO coupling [36]. The common feature of the two types of spin-orbit couplings is that they include coupling through the first-order derivatives with respect to the space coordinate of the BEC components. Contrarily, the appearance of such symmetric sidebands is also referred to as Stokes and anti-Stokes. For some input powers, Stokes and anti-Stokes sidebands can become asymmetric [42], leading to results similar to those in Fig. 5(d).

IV. NUMERICAL EXPERIMENT AND DISCUSSION

The linear stability analysis relies on approximations, making it difficult to table the long-time evolution of the predicted nonlinear patterns. Therefore, the found parameter regions should be used for direct numerical simulations of the generic model to confirm their accuracy. That is performed in this section with application to Eq.(3) via the split-step Fourier method with periodic boundary conditions and time-step $\Delta t = 5 \times 10^{-3}$. As initial conditions, we use the following perturbed CWs:

$$\psi_l(x, y, 0) = \sqrt{n_0} + \epsilon \cos(K_1 x + K_2 y), \quad l = 1, 2, \quad (13)$$

where $n_0 = 1$ and $\epsilon = 10^{-3}$, with the wavenumber $K_1 = K_2 = 2$ for example, for weak values of the photonic SO coupling σ, according to Fig. 2. However, the
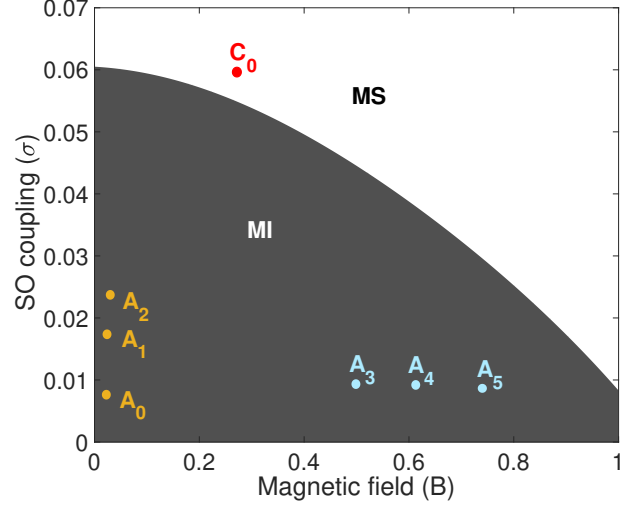
wavenumber may take other values related to instability according to our analytical predictions. Information on pattern formation is recorded in terms of the densities $|\psi_l|^2$ $(l = 1, 2)$, with insistence on the effect related to the TE-TM splitting due to the photonic SO coupling σ, the magnetic field B and the input powers I_1 and I_2.

Before we proceed, let us make the precision that MI's early and nonlinear stages can generate a broad class of analytical solutions of the one-dimensional nonlinear Schrödinger equation referred to as solitons on finite background [43–45]. Among those are the Akhmediev breather, the Kuznetsov-Ma soliton, and the Peregrine soliton. Besides such very rich localized solutions, the dynamical phenomena of polariton instability find their origin in the process of a reservoir-induced MI. Quantum or thermal fluctuations of the condensates or pump noise effects play a crucial role in the static and dynamic properties of homogeneous and inhomogeneous EPCs at finite temperatures. Consequently, a local increase of polariton density induces a local depletion of the reservoir density through spatial hole burning [46, 47]. Concomitantly, when such a local depletion is realized, there is an exponential increase of the initial fluctuation in time, favoured by an inherent attraction of the condensate polaritons in the subsequent potential well. At the end of the process, the density fluctuation is then ejected from
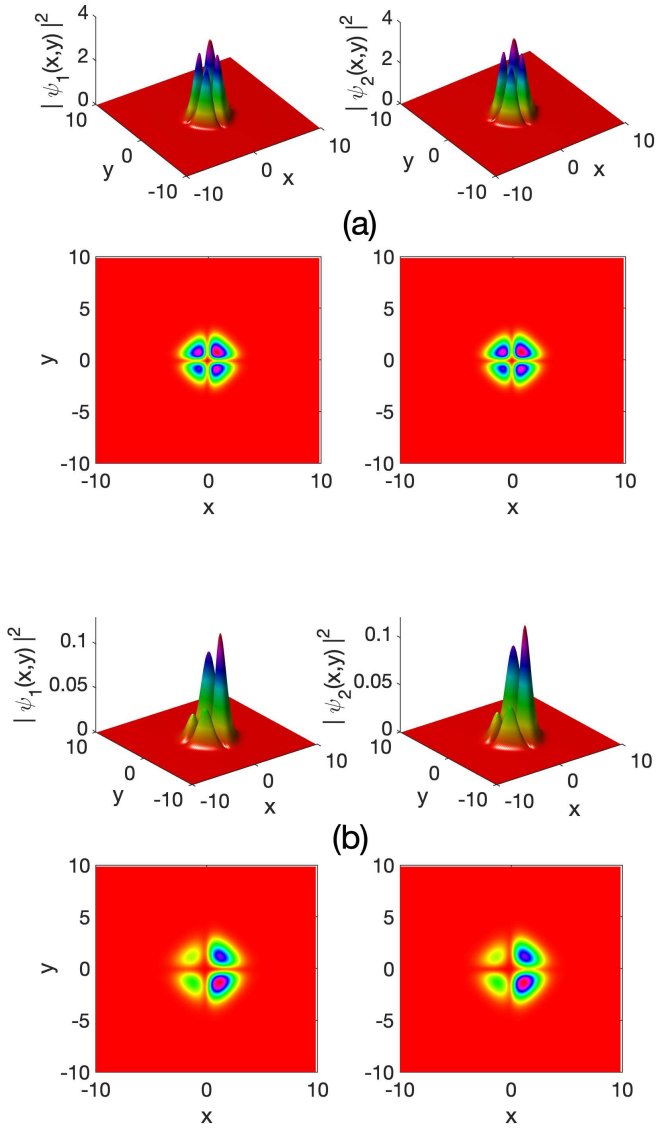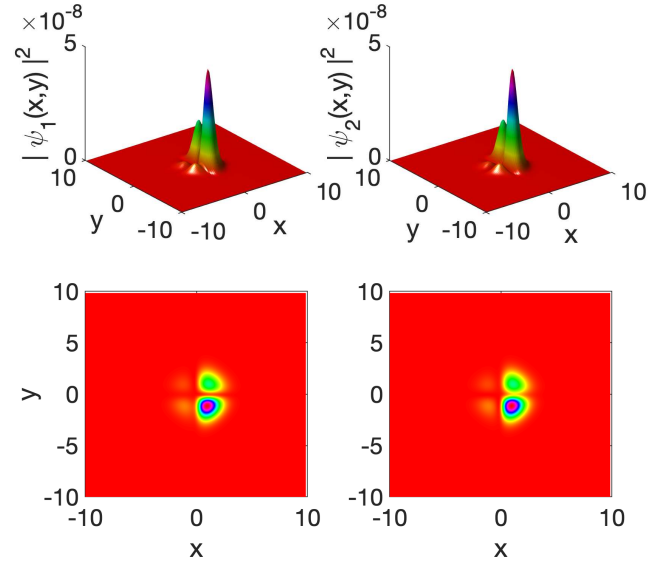
Figure 9. Development of MI using values of σ and B from the point A_5 of the phase diagram of Fig. 7. The left column corresponds to $|\psi_1|^2$, and the right column to $|\psi_2|^2$, along with their corresponding density plots. The other parameter values are: $G = 1.1$, $g = 3.64$, $\tilde{g} = -0.364$, $K_1 = K_2 = 2$, $\Gamma = 3$, $h = -0.1$, and $n_{10} = n_{20} = n_0 = 1$. .
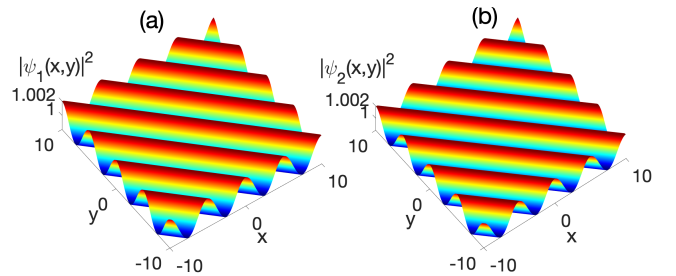

Figure 10. Example of modulational stability (MS) resulting from the point C_0 of the phase diagram of Fig. 7, panels (a) and (b) showing $|\psi_1|^2$ and $|\psi_2|^2$. The other parameter values are: $G = 1.1$, $g = 3.64$, $\tilde{g} = -0.364$, $K_1 = K_2 = 2$, $\Gamma = 3$, $h = -0.1$, and $n_{10} = n_{20} = n_0 = 1$. The left column corresponds to $|\psi_1|^2$, and the right column to $|\psi_2|^2$.

Figure 8. Development of MI, with the panels (a) and (b) showing $|\psi_1|^2$ and $|\psi_2|^2$, and their corresponding density plots obtained from numerical simulations using the points A_3 and A_4 of the phase diagram of Fig. 7. The other parameter values are: $G = 1.1$, $g = 3.64$, $\tilde{g} = -0.364$, $K_1 = K_2 = 2$, $\Gamma = 3$, $h = -0.1$, and $n_{10} = n_{20} = n_0 = 1$. The left column corresponds to $|\psi_1|^2$, and the right column to $|\psi_2|^2$.

its primary position. It starts moving through the condensates due to a positive feedback loop, which is eventually broken by gain saturations and polariton dynamics. The outcome of such a process is the formation of nonlinear patterns, with features closely related to system parameters as shown in the rest of the paper.

The results that show the development of solitonic clusters are depicted in Fig. 6, while the phase diagrams, also obtained from direct numerical simulations, are de-

picted in Fig. 7. The spectrum of behaviors that manifest the development of instability comprises clusters of two counter-symmetric solitons [see Figs. 6(a1) and (a2)] and clusters of four counter-symmetric solitons [see Figs. 6(b1) and (b2)]. For these two types of clusters, the total density leads to clusters of four bright solitons, as shown in Figs. 6(a3) and (b3), where the photonic SO coupling takes the values $\sigma = 0.009$ and $\sigma = 0.018$, respectively. With increasing the SO coupling strength to $\sigma = 0.024$, we obtain the instability features of Fig. 6(c1) and (c2), where the two condensates display similar patterns manifested by clusters of two bright solitons forming diagonal dipoles. Interestingly and expectedly, the
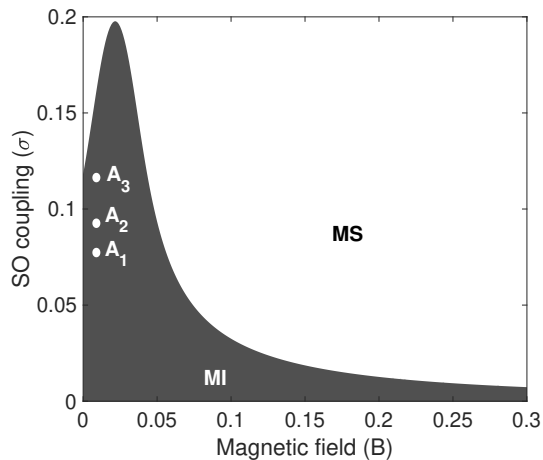
Figure 11. The panels show the numerically generated phase diagrams in the (B, σ)−plane for $I_1 = I_2 = 3$, The wavenumber $K_1 = K_2 = 0.75$, and the initial densities $n_0 = 1$, while the other parameter values are: $G = 1.1$, $g = 3.64$, $\tilde{g} = -0.364$, $\Gamma = 3$, and $h = -0.1$. The points A_1, A_2, and A_3 corresponds to values of B and σ that were used to generate Fig. 12. MI indicates the region of instability, and MS (modulational stability) indicates the region of stability.

total density adheres to the individual instability characteristics.

One factor that does not appear in the expression of the MI growth rate is the magnetic field which affects the system's dynamics. The influence of the magnetic field on confined exciton-polariton modes constitutes a recent debate. The magnetic field is an important component that can be used as a tuning parameter for photon and exciton resonance [48]. Luckily, its effect can be predicted on the emergence of the instability via numerically generated phase diagrams depicted in Fig. 7. For information, the points A_0, A_1, and A_2 in the diagram of Fig. 7(d) are those corresponding to the simulations of Fig. 6, where the magnetic field is relatively weak. For validation, the patterns of Fig. 8(a) and (b) correspond, respectively, to the diagram's points A_3 and A_4. In Fig. 7(a), the generated instability is manifested by a cluster of four compact solitons, and the two condensates display the same dynamics. With increasing the magnetic field B, which corresponds to point A_4, the solitonic clusters become asymmetric due to the annihilation of the two lobes, a situation that gets pronounced in Fig. 9, corresponding to point A_5 of the diagram, where a stronger magnetic field causes the depletion of more solitonic objects from the cluster. The reader should, however, be aware that the linear stability analysis does not permit the prediction of the system's longtime evolution but rather gives information on the onset of instability. That explains why, even though the phase diagrams of Fig. 7, one could not predict the type of solitonic object involved in the manifestation of instability. Moreover, MI instability allows frequency mixing, which is supposed to affect
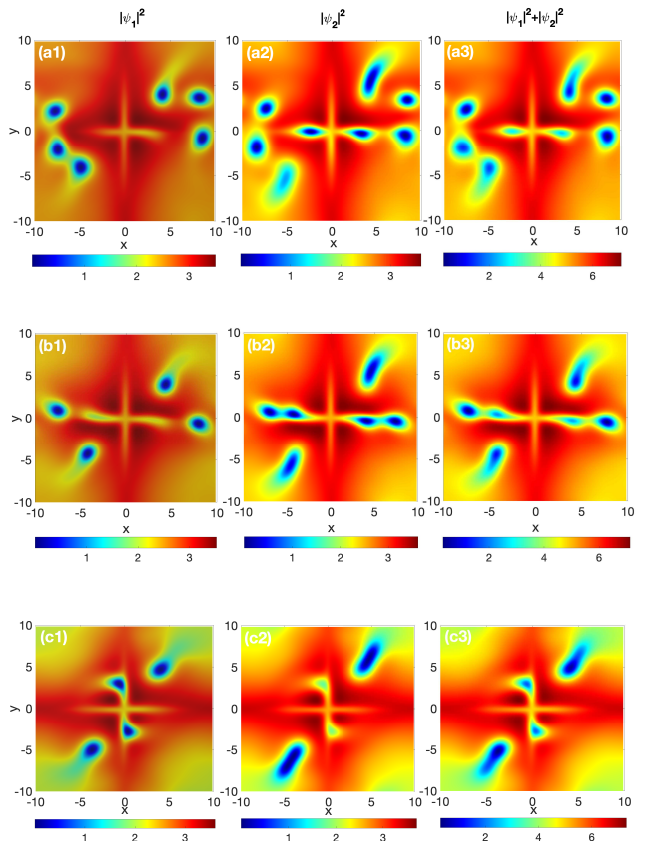

Figure 12. Development of MI, with the panels $(aj)_{j=1,2,3}$, $(bj)_{j=1,2,3}$ and $(cj)_{j=1,2,3}$ corresponding respectively to $\sigma = 0.75$, $\sigma = 0.9$, $\sigma = 0.12$ and the other parameter values being: $I_1 = I_2 = 2$, $G = 1.1$, $g = 3.64$, $\tilde{g} = -0.364$, $K_1 = K_2 = 0.75$, $\Gamma = 3$, $h = -0.1$, $n_{10} = n_{20} = n_0 = 1$, and $B = 0.01$. From left to right, the columns correspond to $|\psi_1|^2$, $|\psi_2|^2$, and $(|\psi_1|^2 + |\psi_2|^2)$.

the dynamics of the obtained patterns as time increases. This gets more pronounced when we deal with a coupled system like the one under study, where there is an energy exchange between the two condensates. This latter phenomenon has been at the origin of the emergence of different kinds of nonlinear patterns in physical systems where there is fair competition between nonlinearity and dispersion. Additional to such effects, the coupled polariton condensates involve the competition between the magnetic field and the photonic SO coupling, which may contribute to enriching their cooperative dynamics under controlled interatomic interactions. Interestingly, for the case where the conditions are not satisfied for MI to develop, the plane wave solutions will remain stable, as shown in Fig. 10, where the obtained patterns have been computed from point C_0 of the phase diagram delivered by Fig. 7. This further agrees well with our analytical predictions.

According to the linear stability analysis and the subsequent growth rate spectrum, different choices of parameters are expected to lead to more exotic behaviors in wave

patterning and propagation. For example, using another set of parameters, mainly the perturbation wavenumbers $K_1 = K_2 = 0.75$, the phase diagram of Fig. 11 is generated against the magnetic field B and the SO coupling strength σ. It is clear that nonlinear patterns will likely occur for a weak or moderate magnetic field, while the highest probability of instability allows even high values of the SO coupling strength. Interestingly, the points A_1, A_2, and A_3 have been used to generate the patterns of Fig. 12. For such points, clusters of deeps, with individual objects similar to dark solitons, are obtained. In Fig. 12(aj)$_{j=1,2,3}$, where $\sigma = 0.075$, the dynamics of the system, through the total density, is driven by the second condensate patterns as shown in Fig. 12(a3). Along the same line, when $\sigma = 0.09$, the number of deeps from individual condensates drops, while the global dynamics of the system is driven by the $|\psi_2|^2$ as depicted in Fig. 12(b3). Finally, under stronger SO coupling, the two components display the same dynamics, drastically reducing the number of defects forming the deep cluster. This confirms the behaviors already reported in Fig. 8.

V. CONCLUSION

In summary, the theory of MI has been utilized to study the emergence of matter waves in nonlinear EPCs. Under the adiabatic approximation, the polariton condensate and the exciton reservoir dynamics have been reduced to a set of coupled 2D CGL equations. Based on the linear stability analysis of CW solutions, we have derived an expression for the MI growth rate, which has been exploited to investigate the roles of pumping powers

and the photonic SO interactions on the MI gain spectrum. Except for the magnetic field that does not contribute to the analytical growth rate of MI, we have found that increasing the photonic SO coupling values brings about additional modes in the growth rate spectrum. Moreover, increasing input power promotes MI growth rate, especially when the strengths of interatomic interactions are suitably tuned. Our analytical predictions have been verified numerically, where a particular interest has been given, primo to the SO coupling strength, with the emergence of solitonic clusters, and, secundo, to the competition between the SO coupling and the magnetic field. Due to the absence of the magnetic field in the expression for the MI growth rate, its effect has been obtained via phase diagrams, computed directly using the 2DCGL equations, that have been utilized to generate more structures, among which clusters of bright solitons and composite clusters of dark solitons also known as deeps. This work opens exciting possibilities in view of investigating novel driven-dissipative nonlinear phenomena with polariton condensates in a controlled platform involving the photonic SO coupling and the magnetic field, among other effects such as the dynamical reservoir regime, multimode dynamics, and instabilities [27, 29, 49].

APPENDICES

Appendix A: Elements of the system's matrix (9)

$$S_1 = \left(\frac{gI_1G}{(\Gamma + Gn_{20})^2} - 1 \right) n_{10}, \quad S_2 = \left(\frac{\tilde{g}I_2G}{(\Gamma + Gn_{20})^2} - h \right) \sqrt{n_{10}n_{20}}, \quad S_3 = \left(\frac{gI_2G}{(\Gamma + Gn_{20})^2} - 1 \right) n_{20},$$

$$S_4 = \left(\frac{\tilde{g}I_1G}{(\Gamma + Gn_{10})^2} - h \right) \sqrt{n_{10}n_{20}}, \quad d = 2i\sigma K_1 K_2, \quad e = i\frac{I_1 n_{10} G}{(\Gamma + Gn_{10})^2}, \quad (A.14)$$

$$f = -\frac{1}{2} \left(K_1^2 + K_2^2 \right), \quad g = \sigma \left(K_1^2 - K_2^2 \right), \quad h = i\frac{I_2 n_{20} G}{(\Gamma + Gn_{20})^2}.$$

Appendix B: Coefficients of the nonlinear dispersion relation (10)

$$P_3 = 2h + 2e, \quad P_2 = 2S_1f - 2S_2g - 2S_3f - 2S_4g + 2d^2 + 4eh - 2f^2 - 2g^2,$$
$$P_1 = -4S_1fh + 4S_2df - 4S_2eg - 4S_3ef - 4S_4df - 4S_4gh$$
$$+ 2d^2e + 2d^2h - 2ef^2 - 2eg^2 - 2f^2h - 2g^2h,$$
$$P_0 = 4S_1S_3f^2 - 4S_1S_g^2 + 2S_1d^2f + 4S_1dh + 2S_1f^3 - 2S_1fg^2 \tag{A.15}$$
$$- 4S_2S_4f^2 + 4S_2S_4g^2 - 2S_2d^2g + 4S_2def - 2S_2f^2g + 2S_2g^3$$
$$- 2S_3d^2f - 4S_3deg + 2S_3f^3 - 2S_3fg^2 - 2S_4d^2g - 4S_4dfh$$
$$- 2S_4f^2g + 2S_4g^3 + d^4 + 4d^2eh + 2d^2f^2 - 2d^2g^2 + f^4 - 2f^4g^2 + g^4$$

[1] J. Kasprzak, M. Richard, S. Kundermann, A. Baas, P. Jeambrun, J. M. J. Keeling, F. M. Marchetti, M. H. Szymanska, R. Andre, J. L. Staehli, V. Savona, P. B. Littlewood, B. Deveaud, and L. S. Dang, Nature (London) **443**, 409 (2006).

[2] N. N. Rosanov, Nature Photon. **6**, 6 (2012).

[3] H. Deng, H. Haug, and Y. Yamamoto, Rev. Mod. Phys. **82**, 1489 (2010).

[4] E. A. Osrovskaya, J. Abdulllaev, A. S. Desyatnikov, M.D. Fraser, and Y. S. Kivshar, Phys. Rev. B **86**, 013636 (2012).

[5] Y. V. Kartashov, V. V. Konotop, and L. Torner, Phys. Rev. Lett. **86**, 205313 (2012).

[6] P. Stepnicki and M. Matuszewski, Phys. Rev. A **88**, 033626 (2013).

[7] V. K. Kalevich, M. M. Afanasiev, V. A. Lukoshkin, D. D. Solnyshkov, G. Malpuech, K. V. Kavokin, S. I. Tsintzos, Z. Hatzopoulos, P. G. Savvidis, and A. V. Kavokin, Phys. Rev. B **91**, 045305 (2015).

[8] Y. G. Rubo, Phys. Rev. Lett. **99**, 106401 (2007).

[9] G. Nardin, K. G. Lagoudakis, M. Wouters, M. Richard, A. Baas, R. Andre, Le Si Dang, B. Pietka, and B. Deveaud-Pledran, Phys. Rev. Lett. **103**, 256402 (2009).

[10] H. Flayac, D. D. Solnyshkov, and G. Malpuech, Phys. Rev. B **83**, 193305 (2011).

[11] T. Byrnes, T. Horikiri,1 N. Ishida, M. Fraser, and Y. Yamamoto, Phys. Rev. B **85**, 075130 (2012).

[12] P. Mietki and M. Matuszewski, Phys. Rev. B **98**, 195303 (2018).

[13] A. Opala, M, Pieczarka, and M. Matuszewski, Phys. Rev. B **98**, 195312 (2018).

[14] S.-C. Cheng and T.-W. Chen, Phys. Rev. E **97**, 032212 (2018).

[15] K. Pawłowski, Ł. A. Turski, Phys. Lett. A **381**, 1710 (2017).

[16] M. Wouters, I. Carusotto, and C. Ciuti, Phys. Rev. B **77**, 115340 (2008).

[17] A. V. Gorbach, B. A. Malomed, and D. V. Skryabin, Phys. Lett. A **373**, 3024 (2009).

[18] T.-W. Chen and S.-C. Cheng, Phys. Rev. E **98**, 032212 (2018).

[19] D. Read, T. C. H. Liew, Y. G. Rubo, A. V. Kavokin, Phys. Rev. B **80**, 195309 (2009).

[20] H. Flayac, I. A. Shelykh, D. D. Solnyshkov, and G. Malpuech, Phys. Rev. B **81**, 045318 (2010).

[21] P. Walker, T. C. H. Liew, D. Sarkar, M. Durska, A. P. D. Love, M. S. Skolnick, J. S. Roberts, I. A. Shelykh, A. V. Kavokin, and D. N. Krizhanovskii, Phys. Rev. Lett. **106**, 257401 (2011).

[22] D. D. Solnyshkov, H. Flayac, and G. Malpuech, Phys. Rev. B **85**, 073105 (2012).

[23] A. Rahimi-Iman, A. V. Chernenko, J. Fischer, S. Brodbeck, M. Amthor, C. Schneider, A. Forchel, S. Höfling, S. Reitzenstein, and M. Kamp, Phys. Rev. B **86**, 155308 (2012).

[24] T. Byrnes, Y. Yamamoto, and P. van Loock, Phys. Rev. B **87**, 201301(R) (2013).

[25] A. V. Yulin, A. V. Nalitov, and I. A. Shelykh, Phys. Rev. B **101**, 104308 (2020).

[26] F. T. Arecchi, J. Bragard, and L. M. Castellano, Opt. Commun. **179**, 156 (1999).

[27] N. Bobrovska and M. Matuszewski, Phys. Rev. B **92**, 035311 (2015).

[28] L. A. Smirnov, D. A. Smirnova, E. A. Ostrovskaya, and Y. S. Kivshar, Phys. Rev. B **89**, 235310 (2014).

[29] N. Bobrovska, E. A. Ostrovskaya, and M. Matuszewski Phys. Rev. B **90**, 205304 (2014).

[30] H. Sigurdsson, I. A. Shelykh, and T. C. H. Liew, Phys. Rev. B **92**, 195409 (2015).

[31] O. A. Smyrnov and F. Biancalana, Phys. Rev. B **83**, 205207 (2011).

[32] H. Saito, and R. Kanamoto, Phys. Rev. Phys. Rev. B **83**, 205207 (2011).

[33] M. Wouters, I. Carusotto, Phys. Rev. Lett. **99**, 140402 (2007).

[34] L. Salasnich, B. A. Malomed, and F. Toigo, Phys. Rev. E **90**, 043202 (2014).

[35] P. Otlaadisa, C. B. Tabi, and T. C. Kofané, Phys. Rev. E **103**, 052206 (2021).

[36] C. B. Tabi, S. Veni, and T. C. Kofané, Phys. Rev. A **104**, 033325 (2021).

[37] C. B. Tabi, H. Tagwo, C. G. L. Tiofack, and T. C. Kofané, Opt. Lett. **47**, 5557 (2022).

[38] A. Canabarro, B. Santos, B. de Lima Bernardo, A. L. Moura,. W. C. Soares, E. de Lima, I. Gléria, and M. L. Lyr, Phys. Rev. A **93**, 023834 (2016).

[39] K. Nithyanandan, R. V. Raja, K. Porsezian, and B. Kalithasan, Phys. Rev. A **86**, 023827 (2012).

[40] X. X. Li, R. J. Cheng, A. X. Zhang, and J. K. Xue, Phys. Rev. E **100**, 032220 (2019).

[41] C. B. Tabi, S. Veni, and T. C. Kofané, Phys. Lett. A **442**, 128192 (2022).

[42] P. Tchofo Dinda, C.M. Ngabireng, K. Porsezian, B. Kalithasan, Optics Commun. **266**, 142 (2006) 142.

[43] N. N. Akhmediev and V. Korneev, Theor. Math. Phys. **69**, 1089 (1986).

[44] N. N. Akhmediev, V. M. Eleonskii, and N. E. Kulagin, Theor. Math. Phys. **72**, 809 (1987).

[45] N. N. Akhmediev, V. I. Korneev, and N. V. Mitskevich, J. Exp. Theoret. Phys. **67**, 159 (1988).

[46] M. Wouters and I. Carusotto, Phys. Rev. Lett. **99**, 140402 (2007).

[47] E. Estrecho, T. Gao, N. Bobrovska, M. Fraser, M. Steger, L. Pfeiffer, K. West, T. Liew, M. Matuszewski, D. Snoke, A. G. Truscott, and E. A. Ostrovskaya, arXiv:1705.00469 (2017).

[48] A. V. Yulin, A. S. Desyatnikov,and E. A. Ostrovskaya, Phys. Rev. B **94**, 134310 (2016).

[49] S. Khan, and H. E. Tureci, Phys. Rev. A **94**, 053856 (2016).